Eur. Phys. J. C 4, 289–299 (1998)
DOI 10.1007/s100529800764

THE EUROPEAN PHYSICAL JOURNAL C
© Springer-Verlag 1998

Radiation zeros at HERA – more about nothing

M. Heyssler[1], W.J. Stirling[1,2]

[1] Department of Physics, University of Durham, Durham, DH1 3LE
[2] Department of Mathematical Sciences, University of Durham, Durham, DH1 3LE

Received: 17 July 1997 / Revised version: 10 September 1997 / Published online: 20 February 1998

Abstract. The process $eq \to eq + \gamma$ exhibits radiation zeros, i.e. configurations of the final–state particles for which the scattering amplitude vanishes. We study these zeros for both e^+u and e^+d scattering. The latter exhibits a type of zero which to our knowledge has not previously been identified. The observability of radiation zeros at HERA is discussed.

1 Introduction

In certain high–energy scattering processes involving the emission of one or more photons, the scattering amplitude vanishes for particular configurations of the final–state particles. Such configurations are known as *radiation zeros*. In the context of high–energy scattering, they were first discussed by Mikaelian, Sahdev and Samuel [1]. To measure the magnetic moment μ_W of the W boson, they proposed and studied the W boson production processes $u\bar{d} \to W^+\gamma$ and $d\bar{u} \to W^-\gamma$. They found that the matrix element vanishes at a particular value of the c.m.s. frame scattering angle $\cos\widehat{\theta}_W = [e_{d(\bar{d})} - e_{\bar{u}(u)}]/[e_{d(\bar{d})} + e_{\bar{u}(u)}] = -1/3$, independent of the photon energy. A similar effect is seen in the $W \to q\bar{q}\gamma$ decay process [2]. Experimentally, these radiation zeros have been observed recently by the CDF collaboration [3] at the Tevatron $p\bar{p}$ collider. There has also been renewed theoretical interest, including studies on double photon emission processes $p\bar{p} \to W^\pm\gamma\gamma \to \ell^\pm\nu\gamma\gamma$ [4] and the uniqueness of radiation zeros to the Standard Model [5]. The energy dependence [6] of radiation zeros in $pp \to \gamma + X$ [7] and using radiation zeros to probe the colour–charge of partons [8] has also been studied. A review of recent developments in the subject can be found in [9].

A first understanding of the phenomenon of radiation amplitude zeros was achieved in the pioneering work of [10]. The vanishing of the scattering amplitude can be understood as arising from complete destructive interference of the classical radiation patterns of the incoming and outgoing charged lines in relativistic n–particle collisions. Taking the single emission of a photon as the paradigm process, it was shown that the amplitudes can vanish if the other particles participating in the process have the same sign of charge e_i.[1]

Same–sign charge scattering occurs naturally in high–energy hadron collisions in subprocesses such as $u\bar{d} \to W^+\gamma$. However similar phenomena can be expected in lepton–hadron collisions, and in particular at HERA in processes such as $eq \to eq + \gamma$ for $eq = e^+u$ or e^-d. Studies of radiation zeros for these processes at HERA were first performed by Bilchak [11], Couture [12], Li, Reid and Samuel [13] and more recently by Doncheski and Halzen [14].

In a recent paper [15] we studied the distributions of soft gluon and photon radiation in $eq \to eq$ scattering at HERA. The motivation was to demonstrate that the radiation patterns are different depending on whether the scattering takes place via standard t–channel γ^*, Z^* exchange or via the production of a new heavy, charged, colour–triplet 'leptoquark' (LQ) resonance in the s channel. Leptoquark production is one of several possible explanations for the apparent excess of high–Q^2 deep inelastic scattering events at HERA [16,17].

A by–product of this study was the identification of radiation zeros in both the Standard Model and leptoquark $e^+q \to e^+q + \gamma$ $(q = u, d)$ scattering amplitudes. For a long–lived resonance ($\Gamma_{\rm LQ} \to 0$) we found radiation zeros for scattering of particles with the same sign (i.e. e^+u scattering in our case) and zeros outside the physical region for e^+d scattering, consistent with the results derived in [11-14]. However we also found that for a short–lived resonance ($\Gamma_{\rm LQ} \to \infty$) *and for the Standard Model* there were radiation zeros also for e^+d scattering within the physical region. Both types of Standard Model $e^+q \to e^+q + \gamma$ radiation zeros will be the focus of the present study.

From an experimental point of view the detection of photons in the final state is highly non–trivial. The rates are small (suppressed by $\mathcal{O}(\alpha)$ compared to the total cross section) and the photons must be well–separated from the beam and from the other final–state particles, and contained within the detector. The basic question is whether the radiation zeros of the scattering amplitude correspond to 'detectable' photons at HERA. In this study we will present results for typical values of the DIS variables y and Q^2 which correspond to observable quark jets and

[1] In fact in general this is only true at tree level, see [10]

scattered positrons. For these values we will investigate the location of the radiation zeros for photons with an energy greater than 5 GeV.

The paper is organised as follows. We first consider soft–photon emission and derive analytic solutions for the location of the radiation zeros in the eq c.m.s. frame. We then show how the transition from soft– to hard–photon emission shifts the position of the zeros. Finally we move to the HERA lab frame to see where the zeros occur in the detector. We also compare our exact matrix–element results with an approximate calculation in which photon emission is included in the collinear approximation, which could correspond for example to a parton–shower implementation of such emission. This model has no radiation zeros and serves as a benchmark for the amplitude suppression in the exact result.

2 Radiation zeros in $eq \to eq\gamma$ scattering

In the following we shall study the reactions

$$e^+(p_1)\, u(p_2) \to e^+(p_3)\, u(p_4) + \gamma(k), \tag{1}$$
$$e^+(p_1)\, d(p_2) \to e^+(p_3)\, d(p_4) + \gamma(k). \tag{2}$$

Other scattering combinations ($e^+\bar{u}, e^-u, \ldots$) can be obtained from these basic processes by readjusting the charge factors. The expression for the matrix element squared (summed and averaged over spins) may for example be obtained by crossing the expression for $e^+e^- \to \mu^+\mu^- + \gamma$ given in [18]. In terms of the four–momenta defined in (1,2) the matrix element for massless quarks and leptons is

$$|\overline{\mathcal{M}}_3|^2(e^+q \to e^+q+\gamma) = e^6 e_q^2 \times \frac{(p_1\cdot p_2)^2 + (p_3\cdot p_4)^2 + (p_1\cdot p_4)^2 + (p_2\cdot p_3)^2}{(p_1\cdot p_3)(p_2\cdot p_4)} \mathcal{F}^\gamma_{\rm SM}, \tag{3}$$

with

$$\frac{1}{2}\mathcal{F}^\gamma_{\rm SM} = e_q^2[24] - e_q\{[12]+[34]-[14]-[23]\} + [13]. \tag{4}$$

We have used here the following short–hand notation for the eikonal factors:

$$[ij] = \frac{p_i\cdot p_j}{(p_i\cdot k)(p_j\cdot k)}. \tag{5}$$

The expression in (4) – the *antenna pattern* of the process – contains collinear ($\mathbf{k}\cdot\mathbf{p}_i \to 0$) as well as infrared ($\omega_\gamma \equiv E_k \to 0$) singularities. It is this factor which vanishes for certain configurations of the momenta. Note that we only take the neutral current γ^*–exchange into account as the antenna pattern in (4) is independent of the exchanged particles as long as they do not themselves emit photons. This approximation will influence the cross section rate slightly at high Q^2, but will not affect the position of the radiation zeros.

2.1 Type 1 radiation zeros

To see under what conditions $\mathcal{F}^\gamma_{\rm SM}$ vanishes, we first recall the 'single–photon theorem' from [10] which states that the amplitude vanishes when the charge–weighted scalar products $Q_i/(p_i\cdot k)$ are equal. If we denote the common value by λ, then

$$[ij] = (Q_iQ_j)^{-1}\lambda^2\, p_i\cdot p_j \tag{6}$$

and it is straightforward to show by substitution in (4) that this gives $\mathcal{F}^\gamma_{\rm SM} = 0$. In the present context, the equality of the charge–weighted scalar products corresponds to

$$\frac{1}{p_1\cdot k} = \frac{e_q}{p_2\cdot k} = \frac{1}{p_3\cdot k} = \frac{e_q}{p_4\cdot k}. \tag{7}$$

We can obtain a simple analytic solution to these equations by taking the soft–photon limit in which $\omega_\gamma/E_i \to 0$. In this limit we have simple two–body kinematics for the quarks and leptons, $p_1 + p_2 = p_3 + p_4$. If we work in the e^+q c.m.s. frame, and define θ_2, θ_4 to be the angle between the photon and the incoming and outgoing quarks respectively, then the equations (7) become

$$\frac{1}{1+z_2} = \frac{e_q}{1-z_2} = \frac{1}{1+z_4} = \frac{e_q}{1-z_4}, \tag{8}$$

where $z_i = \cos\theta_i$. Equivalently,

$$z_2 = z_4 = \frac{1-e_q}{1+e_q}. \tag{9}$$

A necessary condition for such a solution to physically exist is $e_q \geq 0$ ($\Rightarrow |z_i| \leq 1$), i.e. e^+u or $e^+\bar{d}$ scattering. This reproduces the well–known result for scattering of particles with the same sign of electric charge, as discussed in [10]. We call these **Type 1** radiation zeros. By itself, however, the condition $e_q \geq 0$ is not sufficient to guarantee a zero in the scattering amplitude. The equation $z_2 = z_4$ can only be satisfied for certain configurations of the final–state particles. To see this, we introduce an explicit representation of the c.m.s. four–momenta:

$$p_1^\mu = \frac{\sqrt{\hat{s}}}{2}(1,0,0,-1), \tag{10}$$
$$p_2^\mu = \frac{\sqrt{\hat{s}}}{2}(1,0,0,1), \tag{11}$$
$$p_4^\mu = \frac{\sqrt{\hat{s}}}{2}(1,\sin\Theta_q,0,\cos\Theta_q), \tag{12}$$
$$p_3^\mu = \frac{\sqrt{\hat{s}}}{2}(1,-\sin\Theta_q,0,-\cos\Theta_q), \tag{13}$$
$$k^\mu = \omega_\gamma(1,\sin\theta_\gamma\cos\phi_\gamma,\sin\theta_\gamma\sin\phi_\gamma,\cos\theta_\gamma). \tag{14}$$

These variables are illustrated in Fig. 1. It is straightforward to show that the conditions for $\mathcal{F}^\gamma_{\rm SM} = 0$ defined in (9) correspond to

$$\cos\widehat{\theta}_\gamma = \frac{1-e_q}{1+e_q}, \tag{15}$$

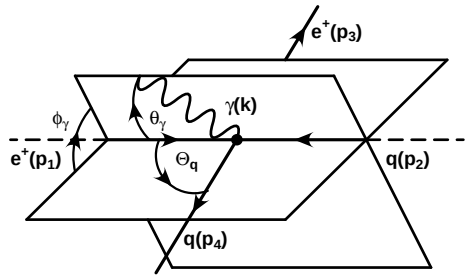

Fig. 1. Parametrisation of the kinematics for $e^+(p_1)q(p_2) \to e^+(p_3)q(p_4)+\gamma(k)$ scattering in the e^+q c.m.s. frame. The orientation of the photon relative to the scattering plane is denoted by θ_γ and ϕ_γ

and

$$\widehat{\phi}_\gamma = \pm \arccos\left(\frac{\tan(\Theta_q/2)}{\tan\widehat{\theta}_\gamma}\right). \tag{16}$$

Thus for $e_u = +2/3$ we find radiation zeros at $\widehat{\theta}_\gamma \simeq 78.46^\circ$ and for $e_{\bar{d}} = +1/3$ at $\widehat{\theta}_\gamma = 60^\circ$. We present the positions of the radiation zeros $(\widehat{\phi}_\gamma, \widehat{\theta}_\gamma)$ for process (1) (e^+u scattering) in Fig. 2a. Note that the requirement of a physical solution for $\widehat{\phi}_\gamma$ places restrictions on Θ_q. There are two radiation zeros in the $(\phi_\gamma, \theta_\gamma)$ plane for $\Theta_q < 2\widehat{\theta}_\gamma \simeq 156.94^\circ$. The cones around the incoming and outgoing quarks defined by $z_2, z_4 = 1/5$ have two lines of intersection along which there is completely destructive interference of the radiation. Note also that at $\Theta_q = 2\widehat{\theta}_\gamma = \Theta_q^{\rm crit}$ the radiation zeros degenerate to a single line (i.e. single point in $(\phi_\gamma, \theta_\gamma)$ space) located in the scattering plane ($\widehat{\phi}_\gamma = 0^\circ$). There are no radiation zeros for $\Theta_q > 2\widehat{\theta}_\gamma \simeq 156.94^\circ$. Finally, for $\Theta_q = 0^\circ$ there is an infinite number of radiation zeros ('null zone') located on a cone around the beam line with opening angle $\widehat{\theta}_\gamma$.

2.2 Type 2 radiation zeros

The processes (1,2) exhibit a second class of radiation zeros, which we call **Type 2**, which do not satisfy the 'single–photon theorem'. These zeros are located in the scattering plane at $\widehat{\phi}_\gamma = 0^\circ$ and $\widehat{\phi}_\gamma = 180^\circ$. The corresponding $\widehat{\theta}_\gamma$ values may be calculated straightforwardly in the soft–photon approximation as a function of the quark charge e_q and the quark scattering angle Θ_q. The result is

$$\cos\widehat{\theta}_\gamma = \frac{1}{2}\frac{\left(1-e_q^2\right)\left(1+\cos\Theta_q\right) \pm \sqrt{\Delta_\gamma\left(e_q, \cos\Theta_q\right)}}{\left(1-e_q\right)^2}, \tag{17}$$

with

$$\Delta_\gamma\left(e_q, \cos\Theta_q\right) = \left[\left(e_q^2-1\right)\left(1+\cos\Theta_q\right)\right]^2 - 4\left(1-e_q\right)^2\left(e_q^2\cos\Theta_q + 2e_q + \cos\Theta_q\right). \tag{18}$$

Table 1. Ranges of the quark scattering angle Θ_q, for different quark charges, for which radiation zeros exist. Note that for $e_q < 0$ there are always two radiation zeros in the scattering plane for $\widehat{\phi}_\gamma = (0^\circ, 180^\circ)$ with the $\widehat{\theta}_\gamma$ value given by (17)

e^+u	$e_q = +2/3$	$\cos\Theta_q \le \pi - \arccos\left(\frac{23}{25}\right)$	$\Theta_q \gtrsim 157^\circ$
$e^+\bar{d}$	$e_q = +1/3$	$\cos\Theta_q \le -\frac{1}{2}$	$\Theta_q \ge 120^\circ$
e^+d	$e_q = -1/3$	$\forall\ \cos\Theta_q$	$\forall\ \Theta_q$
$e^+\bar{u}$	$e_q = -2/3$	$\forall\ \cos\Theta_q$	$\forall\ \Theta_q$

The condition $\Delta_\gamma\left(e_q, \cos\Theta_q\right) \ge 0$ constrains the range of e_q for which physical zeros exist. In terms of the polar angle Θ_q we have

$$-\infty < e_q \le \frac{\cos\Theta_q + 3 - 2\sqrt{2(1+\cos\Theta_q)}}{1-\cos\Theta_q} \le 1, \tag{19}$$

or

$$1 \le \frac{\cos\Theta_q + 3 + 2\sqrt{2(1+\cos\Theta_q)}}{1-\cos\Theta_q} \le e_q < +\infty, \tag{20}$$

the latter being actually redundant since Standard Model quarks have $|e_q| \le +2/3$. From (19) we obtain constraints on the quark scattering angle Θ_q for particular flavours of quark. There are radiation zeros for all $e_q < 0$ and for positively charged quarks in a limited range of Θ_q. We summarise the results in Table 1. Note that e^+u scattering has both Type 1 and 2 zeros. However, the latter are located very close to the beam direction, making their observation difficult in practice. They also require very high Q^2 (back–scattered quarks) and therefore have a small event rate. The positions of the Type 2 zeros for e^+d scattering are shown in Fig. 2b as a function of Θ_q. Finally, Table 2.2 lists the numerical values of the radiation zero angles $(\widehat{\phi}_\gamma, \widehat{\theta}_\gamma)$ for several values of Θ_q.

2.3 Radiation zeros for arbitrary photon energies

The analytic results obtained above use the soft–photon approximation. However radiation zeros of both types exist for *all* photon energies and can be located using numerical techniques[2]. We continue to work in the e^+q c.m.s. frame but now use exact $2 \to 3$ kinematics. Without any essential loss of generality, we can keep the direction (Θ_q) and the energy (E_q') of the outgoing quark fixed and vary the direction and energy of the outgoing photon, constructing simultaneously the four–momentum of the outgoing positron to conserve energy and momentum.

[2] Note that we use massless quarks and leptons to calculate the matrix elements. However both types of radiation zero are also present for non–zero masses [19]

Table 2. Position of the radiation zeros $(\widehat{\phi}_\gamma, \widehat{\theta}_\gamma)$ for three different quark scattering angles Θ_q, in the soft–photon approximation

Θ_q	e^+d scattering		e^+u scattering	
30°	$(0°, 76.12°)$	$(180°, 46.12°)$	$(-86.86°, 78.46°)$	$(86.86°, 78.46°)$
45°	$(0°, 84.98°)$	$(180°, 39.98°)$	$(-83.23°, 78.46°)$	$(83.23°, 78.46°)$
90°	$(0°, 114.29°)$	$(180°, 24.29°)$	$(-78.22°, 78.46°)$	$(78.22°, 78.46°)$

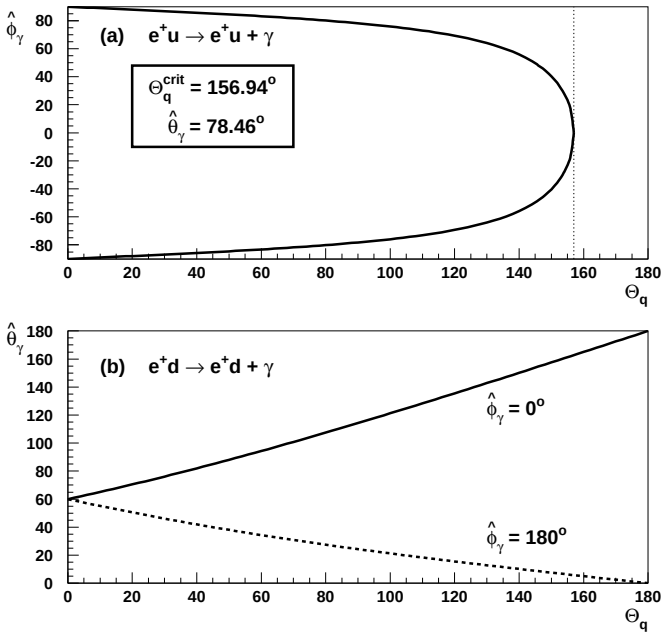

Fig. 2. The position of the radiation zeros as a function of the quark scattering angle Θ_q for soft–photon emission in **a** $e^+u \to e^+u + \gamma$ and **b** $e^+d \to e^+d + \gamma$ in the $(\phi_\gamma, \theta_\gamma)$ c.m.s. phase space of the soft photon

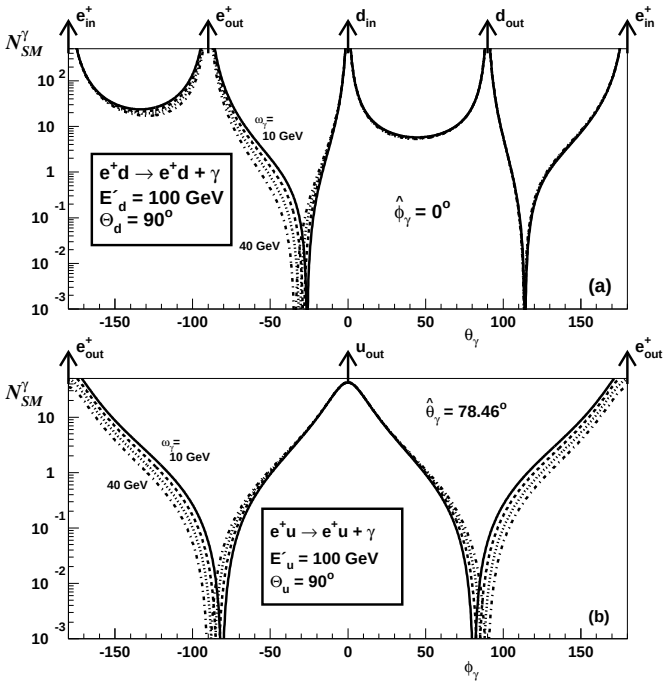

Fig. 3. The dimensionless antenna pattern $\mathcal{N}^\gamma_{\rm SM} = \omega_\gamma^2 \mathcal{F}^\gamma_{\rm SM}$ for **a** $e^+d \to e^+d + \gamma$ (at fixed $\widehat{\phi}_\gamma = 0°$) and **b** $e^+u \to e^+u + \gamma$ (at fixed $\widehat{\theta}_\gamma \simeq 78.46°$) for different photon energies ($\omega_\gamma = 10, 20, 30, 40$ GeV). The outgoing quark direction is fixed at $\Theta_q = 90°$ with energy $E'_q = 100$ GeV. The directions of the incoming and outgoing quarks and leptons are indicated

The new four–vectors of the outgoing quark, lepton and photon momenta are then

$$p_4^\mu = E'_q\,(1, \sin\Theta_q, 0, \cos\Theta_q)\,, \tag{21}$$
$$p_3^\mu = p_1^\mu + p_2^\mu - p_4^\mu - k^\mu, \tag{22}$$
$$k^\mu = \omega_\gamma\,(1, \sin\theta_\gamma\cos\phi_\gamma, \sin\theta_\gamma\sin\phi_\gamma, \cos\theta_\gamma)\,. \tag{23}$$

Once again we obtain a vanishing matrix element in (3) if the antenna pattern $\mathcal{F}^\gamma_{\rm SM}$ of (4) is zero. For Type 1 radiation zeros, the single–photon theorem again leads to the conditions in (7). The equality of $p_1 \cdot k$ and $p_2 \cdot k$ leads immediately to (15), i.e. the radiation zeros are at fixed $\widehat{\theta}_\gamma$ *independent of the photon energy*. However the azimuthal angle $\widehat{\phi}_\gamma$ does vary with ω_γ, since the supplementary condition $z_2 = z_4$ only applies in the $\omega_\gamma \to 0$ limit. For Type 2 zeros, it can be shown that the condition $\widehat{\phi}_\gamma = 0°, 180°$ again applies for arbitrary ω_γ, i.e. the zeros are always located in the scattering plane.

In Fig. 3 we show the dimensionless quantity $\mathcal{N}^\gamma_{\rm SM} = \omega_\gamma^2 \mathcal{F}^\gamma_{\rm SM}$ for different photon energies and fixed final–state quark kinematics. The figures (a) and (b) correspond respectively to slices through the $(\phi_\gamma, \theta_\gamma)$ plane according to the positions of the soft–photon Type 1 and 2 radiation zeros of the previous sections. As the photon energy increases, there is a systematic shift in the positions of the zeros. As radiation zeros are semi–classical effects due to destructive interference, it is easy to understand that fixing the position of the outgoing quark and simultaneously increasing ω_γ shifts the interference regions be-

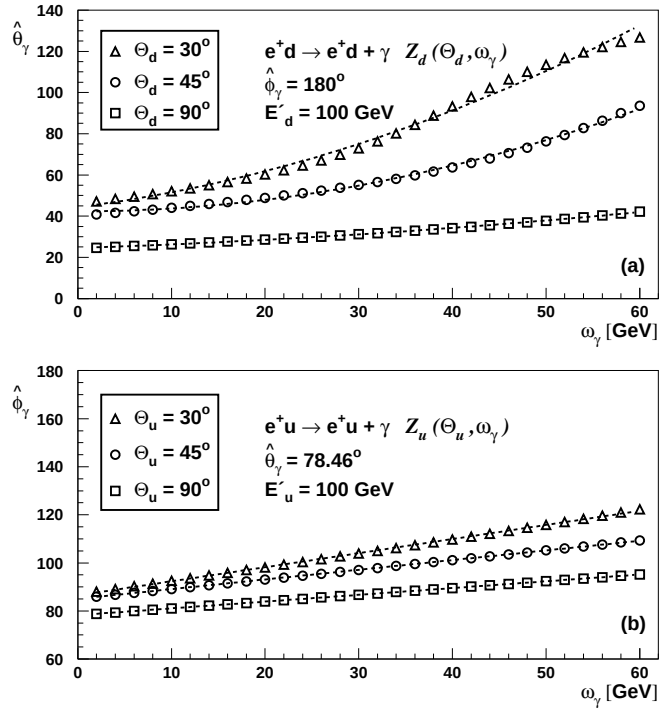

Fig. 4. The positions of the radiation zeros $\mathcal{Z}_q$ as a function of the quark scattering angle Θ_q and the photon energy ω_γ for **a** e^+d scattering and **b** e^+u scattering. The analytic results for the soft–photon limit ($\omega_\gamma \to 0$) are summarised in Table 2.2. The *dashed lines* are a polynomial fit in the photon energy for given Θ_q. Note that in **a** we employ a second–order fit whereas in **b** a first–order fit is sufficient. The fit parameters are listed in the text

tween the participating charged particles as the outgoing positron must balance energy and momentum and thus changes its relative orientation. Thus the asymmetric ω_γ dependence of the two radiation zeros in Fig. 3a is due simply to our choice of fixing the final–state quark direction rather than the direction of the scattered positron. The zero in the quadrant between the (fixed) incoming positron and outgoing quark directions is relatively insensitive to the changes in the positron direction induced by varying ω_γ. The other zero follows the direction of the outgoing positron as ω_γ increases. The same effect also explains the symmetric dependence of the two radiation zeros for the process $e^+u \to e^+u+\gamma$. The zeros are located symmetrically above and below the scattering plane and are influenced equally by changes in the scattered positron direction.

Figures 4a,b show the positions[3] of the radiation zeros $\mathcal{Z}_d$ and $\mathcal{Z}_u$ for the two processes as a function of the photon energy at various fixed Θ_q. $\mathcal{Z}_d(\Theta_d, \omega_\gamma)$ is located in the quadrant between the outgoing positron and the incoming d quark and $\mathcal{Z}_u(\Theta_u, \omega_\gamma)$ is located in the quadrant between the outgoing u quark and the outgoing positron

[3] The exact locations of the zeros are determined by a numerical procedure

Table 3. Fits for the ω_γ dependence of the two selected radiation zeros shown in Figs. 4a,b according to the definitions given in (24, 25)

	d–quarks			u–quarks	
Θ_q	d_1	d_2	χ^2	u_1	χ^2
30°	0.576	0.015	5.91	0.59	5.3×10^{-2}
45°	0.012	0.014	0.76	0.40	3.0×10^{-3}
60°	0.149	0.002	0.01	0.28	1.3×10^{-4}

(see Figs. 3a,b). The values on the axes at $\omega_\gamma = 0$ coincide with the analytic results obtained previously (see Table 2.2).

The dashed lines in Figs. 4a,b are simple polynomial fits. For e^+d scattering we fit $\widehat{\theta}_\gamma$ for fixed $\widehat{\phi}_\gamma = 180°$ using a quadratic polynomial,

$$\mathcal{Z}_d(\Theta_d, \omega_\gamma) = \mathcal{Z}_d^0(\Theta_d) + d_1\omega_\gamma + d_2\omega_\gamma^2, \qquad (24)$$

where $\mathcal{Z}_d^0(\Theta_d)$ corresponds to the soft–photon results listed in Table 2.2. The radiation zeros for e^+u scattering (i.e. a fit for $\widehat{\phi}_\gamma$ at fixed $\widehat{\theta}_\gamma = 78.46°$) can be approximated by a first–order polynomial

$$\mathcal{Z}_u(\Theta_u, \omega_\gamma) = \mathcal{Z}_u^0(\Theta_u) + u_1\omega_\gamma. \qquad (25)$$

The results of the fit are presented in Table 3.

As a final exercise in our c.m.s. studies we calculate the differential cross section for the two subprocesses. The general form of the differential subprocess cross section in the e^+q c.m.s. frame may be written as

$$\frac{d^2\hat{\sigma}}{d\Omega_\gamma d\Omega_q}(eq \to eq+\gamma) = \frac{2}{(4\pi)^5}\int\limits_{\omega_\gamma^{\rm cut}} d\omega_\gamma \, \frac{E_q'^2\omega_\gamma}{\hat{s}^{3/2}|\sqrt{\hat{s}}/2 - \omega_\gamma|} \times|\overline{\mathcal{M}}_3|^2(eq \to eq+\gamma), \qquad (26)$$

where

$$E_q' = \frac{\hat{s} - 2\sqrt{\hat{s}}\omega_\gamma}{2\sqrt{\hat{s}} - 2\omega_\gamma(1-\cos\theta_{q\gamma})}. \qquad (27)$$

The integration over ω_γ smears out the radiation zeros to form a sharp *dip* in the cross section. Since the cross section decreases rapidly with increasing ω_γ, the dip is close to the location of the zero corresponding to fixed $\omega_\gamma = \omega_\gamma^{\rm cut}$. The distributions for the two subprocesses are shown in Figs. 5a,b for $\omega_\gamma^{\rm cut} = 5$ GeV. Note that we have also imposed an angular cut around the beam line of 5° in Fig. 5a. The transition from radiation zeros to radiation dips can be seen by comparing Figs. 4 and 5. Choosing larger values of $\omega_\gamma^{\rm cut}$ shifts the radiation dips to higher values of $\widehat{\phi}_\gamma$ and $\widehat{\theta}_\gamma$ at the same time decreasing the overall value of the subprocess cross section.

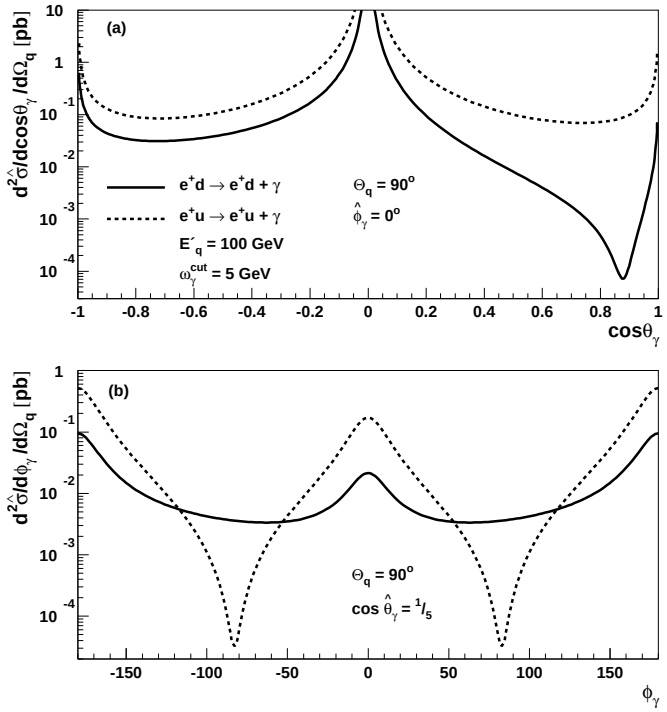

Fig. 5. The subprocess differential cross section $d^2\hat{\sigma}/d\Omega_\gamma d\Omega_q$ of (26) for c.m.s. e^+d scattering (*solid lines*) and e^+u scattering (*dashed lines*). We again choose those slices through the photon parameter space $(\phi_\gamma, \theta_\gamma)$ that contain radiation zeros in the soft limit (i.e. a choice of $\widehat{\phi}_\gamma = 0°$ in **a** and $\cos\widehat{\theta}_\gamma = 1/5$ in **b**). Note that we integrate over the photon energy ω_γ and fix the position of the outgoing quark at $\Theta_q = 90°$ with energy $E'_q = 100$ GeV. In **a** we impose an additional angular cut of 5° around the beam line

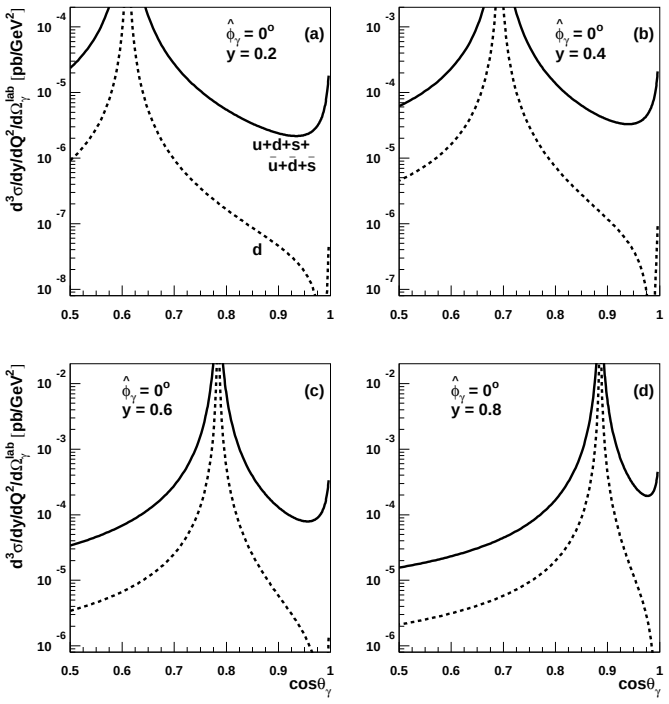

Fig. 6. The positions of the radiation dips for the process $e^+d \to e^+d + \gamma$ (*dashed lines*) for different values of y for $\theta_\gamma \in [5°, 60°]$ (hemisphere of outgoing e^+). A cut of 5° around the beam line is imposed. The radiation zeros and thus the radiation dips for this process are again located within the plane $(\widehat{\phi}_\gamma = 0°)$. The Q^2 value is 10^4 GeV^2. The *solid lines* show the sum of the contributions from u, d, s quarks and antiquarks. The divergences in the plots show the positions of the outgoing e^+ at $\cos\theta_\gamma = \cos\Theta_e^{\rm lab}$ with the values for $\Theta_e^{\rm lab}$ given in Table 4

3 Radiation zeros at HERA

In this section we shall discuss the possible observation of radiation zeros at HERA. To do this we modify the previous calculation by (a) moving to the HERA lab frame, (b) including the parton distribution functions, and (c) summing over all flavours of quarks in the initial state.

In neutral current DIS the cleanest way to reconstruct the kinematics of a given event is by measuring the energy E'_e and the laboratory angle $\Theta_e^{\rm lab}$ of the outgoing positron. In terms of the Bjorken scaling variables x and y we may write (see for example [20,21])

$$y = 1 - \frac{E'_e}{2E_e}\left(1 - \cos\Theta_e^{\rm lab}\right), \tag{28}$$

$$x = \frac{1}{y}\frac{E'_e}{2E_p}\left(1 + \cos\Theta_e^{\rm lab}\right), \tag{29}$$

$$Q^2 = xys, \tag{30}$$

where E_p is the energy of the incoming proton and $s = 4E_eE_p$ is the c.m.s. energy of the e^+p system. The polar angle of the positron $\Theta_e^{\rm lab}$ is defined with respect to the incident proton beam direction. The precision of the y measurement typically degrades as $1/y$, and thus one naturally assumes $y \gtrsim 0.05$ [21].

Since we are interested in DIS events with an additional hard photon emitted at different angles in phase space, the natural quantity to consider is the triple–differential cross section $d^3\sigma/dydQ^2d\Omega_\gamma^{\rm lab}$. In the HERA lab frame this is given by

$$\frac{d^3\sigma}{dydQ^2d\Omega_\gamma^{\rm lab}}(e+p \to e+q+\gamma+X)$$
$$= \frac{1}{256\pi^4 s}\sum_q \int\limits_{\omega_\gamma^{\rm cut}} d\omega_\gamma \, \frac{\omega_\gamma}{\xi_q(Q^2/x - 2p\cdot k)}$$
$$\times |\overline{\mathcal{M}}_3|^2(eq \to eq+\gamma)\; f_{q/p}(\xi_q, Q^2), \tag{31}$$

where

$$\xi_q = \frac{Q^2 - 2q\cdot k}{Q^2/x - 2p\cdot k} \geq x. \tag{32}$$

In the calculations which follow we choose $E_e = 27.5$ GeV, $E_p = 820$ GeV and neglect all quark and lepton masses. We again take $\omega_\gamma^{\rm cut} = 5$ GeV for the lower limit of the photon energy. For the quark distribution functions $f_{q/p}(\xi_q, Q^2)$

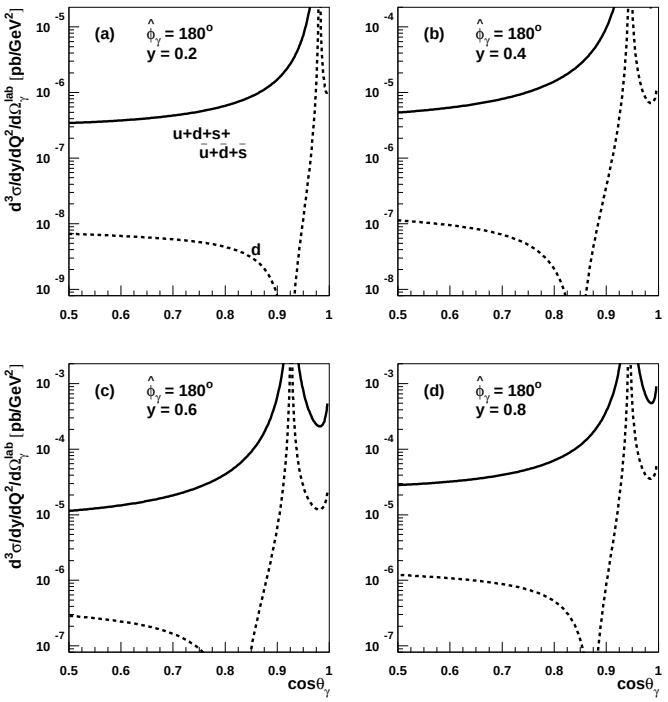

Fig. 7. The positions of the radiation dips for the process $e^+d \to e^+d+\gamma$ (*dashed lines*) for different values of y for $\theta_\gamma \in [5^\circ, 60^\circ]$ (the hemisphere of the outgoing quark). A cut of 5° around the beam line is imposed. Note that $\widehat{\phi}_\gamma = 180^\circ$

Table 4. Typical values of the scattered positron energy and angle for our parameter choice $Q^2 = 10^4$ GeV^2 and different values of y

y	x	$\Theta_e^{\rm lab}$	E'_e
0.20	0.55	52.4°	112.9 GeV
0.40	0.27	46.2°	107.4 GeV
0.60	0.18	38.4°	101.9 GeV
0.80	0.14	27.6°	96.4 GeV

we use the MRS(A′) set of partons introduced in [22], with QCD scale parameter $\Lambda^{N_f=4}_{\overline{\rm MS}} = 231$ MeV corresponding to $\alpha_s(M_Z^2) = 0.113$. In order to stay in the valence–quark scattering region (i.e. large ξ_q), where we expect the radiation zeros to be most visible, we choose $Q^2 = 10^4$ GeV^2 and $y \in [0.1, 1.0]$. Typical values for x and the positron variables $\Theta_e^{\rm lab}$ and E'_e are listed in Table 4.

As we move from the e^+q c.m.s. frame to the HERA lab frame, all four–momenta are boosted along the beam direction. Although this has no effect on the azimuthal angles, the polar angles and hence the locations of all radiation zeros, in particular $\widehat{\theta}_\gamma$, are changed. The simplest consequence of this is that the e^+d radiation scattering zeros remain located in the scattering plane at $\widehat{\phi}_\gamma = 0^\circ$ and 180°. To find the locations of the radiation zeros for process (2) we therefore fix $\widehat{\phi}_\gamma = 0^\circ$ and numerically determine their positions in θ_γ.

3.1 Radiation zeros for d quark scattering

In Fig. 6 we present the cross section of (31) for the process $e^+ + p \to e^+ + {\rm jet} + \gamma + X$ via $e^+d \to e^+d+\gamma$ scattering (dashed line) as well as via the sum over all subprocesses $e^+q \to e^+q+\gamma$ with $q = u, d, s, \bar{u}, \bar{d}$ and $\bar{s}$. We have chosen to focus on the radiation zero located between the incoming quark and outgoing positron. We fix $Q^2 = 10^4$ GeV^2 and vary y from $y = 0.2$ in Fig. 6a to $y = 0.8$ in Fig. 6d, which corresponds to x values in the region $0.1 < x < 0.6$ (cf. Table 4). Again we observe radiation dips instead of radiation zeros due to the integration over the photon energy. Increasing y pulls the radiation dips closer to the beam line and thus makes their observation more difficult. Already at $y = 0.2$ the e^+d radiation dip in Fig. 6a is only about 14° ($\cos\widehat{\theta}_\gamma \simeq 0.97$) from the beam line, and gets even closer with increasing y. Note that we impose a cut of 5° around the beam line. Increasing y means decreasing the polar angle of the outgoing positron $\Theta_e^{\rm lab}$ (cf. Table 4). Thus the zone of destructive interference approaches the beam line as the e^+ approaches the beam line. The conclusion is that observation of the radiation dips in the sector between the incoming quark and outgoing e^+ in high–Q^2 events is only possible for small values of y.

The second radiation zero we found in our studies was located between the incoming positron and the outgoing quark. In Fig. 7 we display this region again for processes only involving d quarks (dashed lines) as well as for processes involving all light quark and antiquark flavours. The obvious singularities in Figs. 7a–d are caused by collinearity of the photon with the outgoing quark. Now the problem is that the zeros are close (always within 10°) to the outgoing quark jet, even though the radiation dips here are well separated from the beam line ($\simeq 35^\circ$ for $y = 0.6$).

A more serious problem evident in Figs. 6 and 7 is the enormous background from the other quark scattering subprocesses, which completely fills in the radiation dip. We observe a ratio (away from the singularities) of signal/background $\simeq 1/(200-300)$. The dominance of the u quark contribution is striking. For the given values of x and thus ξ_q (cf. (32)) we find the following ratios for the MRS(A′) parton distributions at $Q^2 = 10^4$ GeV^2:

$$\xi_q = 0.1: \quad \to u(\xi_q) : d(\xi_q) : \bar{d}(\xi_q) : \bar{u}(\xi_q) \simeq 100 : 60 : 22 : 15, \tag{33}$$

$$\xi_q = 0.6: \quad \to u(\xi_q) : d(\xi_q) : \bar{d}(\xi_q) : \bar{u}(\xi_q) \simeq 100 : 17 : 1 : 1. \tag{34}$$

In addition to these parton distribution factors there are the usual quark charge squared (e_q^2) factors from the leading order $eq \to eq$ scattering, which further enhance the u–quark contribution. Note that the s–quark contribution

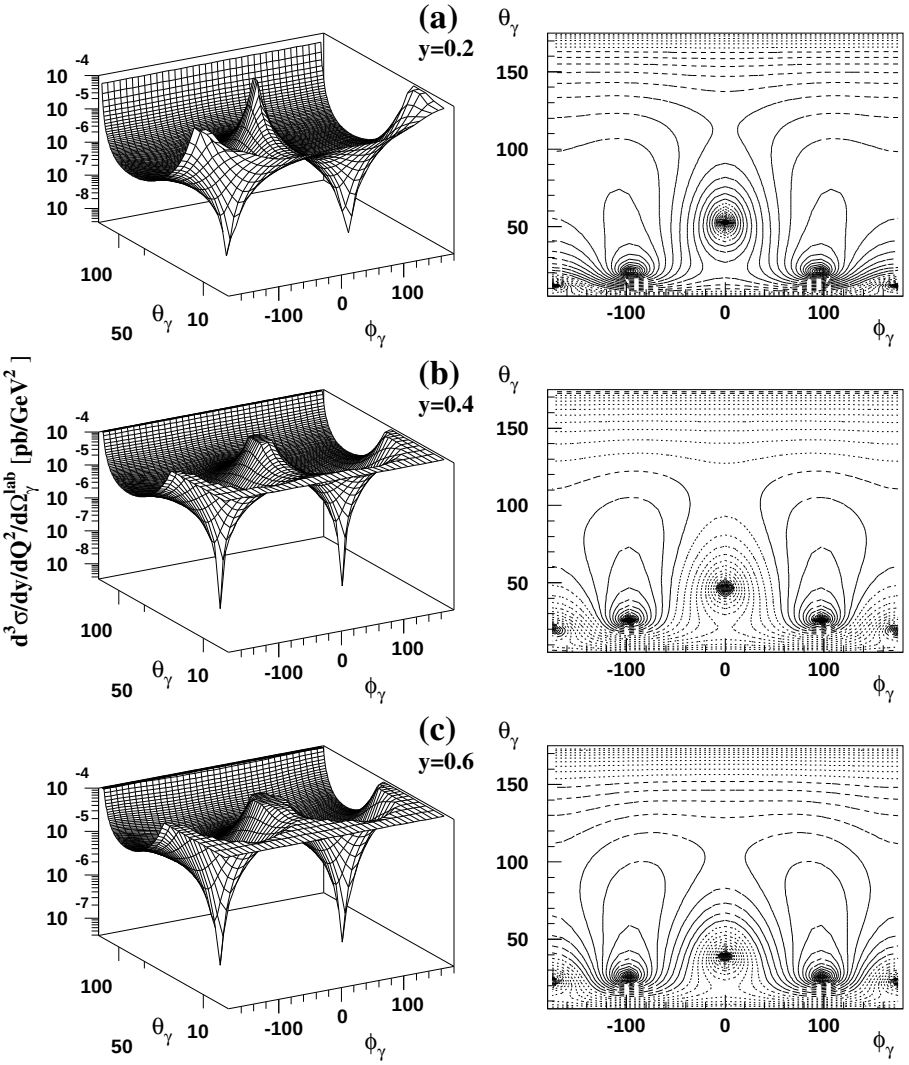

Fig. 8. The differential cross section of (31) for the process $e^+u \to e^+u+\gamma$ in the $(\phi_\gamma, \theta_\gamma)$ phase space of the emitted photon. The corresponding contour plots are shown on the right–hand side. For fixed $Q^2 = 10^4$ GeV^2 we vary y (defined in (28)) from $y = 0.2$ in **a** and $y = 0.4$ in **b** to $y = 0.6$ in **c**. The kinematic variables x, E'_e and $\Theta_e^{\rm lab}$ for each y value can be read off from Table 4. Note that we introduce in the surface plots on the left–hand side a logarithmic scale in θ_γ. The radiation dips are symmetric in ϕ_γ. Again we impose a 5° cut around the beam line, and thus $\theta_\gamma \in [5^\circ, 175^\circ]$

plays a minor role; it is roughly 70% of the $\bar{u}$ contribution at $\xi_q = 0.1$ and comparable to the latter at higher values of ξ_q. Even though d, s and $\bar{u}$ quarks all yield radiation dips in the scattering plane (the d– and s–quark zeros coincide) none of these are likely to be observable. The only possibility might be to try to flavour–tag the d or s quark jets, for example by selecting only those jets with a leading negatively charged track.

3.2 Radiation zeros for u quark scattering

According to the parton distribution hierarchy presented in the previous section we might expect that the Type 1 radiation zeros, which we identified with the *traditional* radiation zeros already discussed in the literature, are the most promising for detection. We recall that in the soft–photon limit and in the c.m.s. frame these zeros are located at fixed polar angle $\cos\widehat{\theta}_\gamma = 1/5$ (cf. (15)). Their position in ϕ_γ may then be directly computed using (16). We found that they are located well outside the scattering plane (except for $\Theta_q = 2\widehat{\theta}_\gamma = 2\cos^{-1}(1/5)$) as discussed earlier. Integrating over the photon energy ω_γ and using exact $2 \to 3$ kinematics slightly shifts the position of the corresponding radiation dips. The ω_γ dependence for different kinematical situations was shown in Fig. 4b.

Moving to the HERA lab frame boosts the polar angles and changes the position of the radiation dips for $e^+u \to e^+u+\gamma$. In Figs. 3a–c we show the differential cross section of (31) for this process over the full $(\phi_\gamma, \theta_\gamma)$ space. As before we fix $Q^2 = 10^4$ GeV^2 and chose the three y values: 0.2, 0.4 and 0.6. We impose cuts of 5° around the beam line (by definition located at $\theta_\gamma = 0^\circ$ and 180°) and cut the differential cross section at $d\sigma < 10^{-4}$ pb/GeV^2 to avoid the collinear singularities along the directions of the outgoing e^+ (located at $\phi_\gamma = 0^\circ$) and the outgoing u quark (at $\phi_\gamma = \pm 180^\circ$). We see that the positions of the zeros are still symmetric in ϕ_γ, as expected. Note that since the collinear singularities and the radiation dips tend to concentrate around small values of θ_γ, we have introduced

a logarithmic scale for θ_γ in the three–dimensional plots of Fig. 3.

We can numerically locate the positions of the radiation dips in the $(\phi_\gamma, \theta_\gamma)$ phase space for our different choices of y:

$$\begin{aligned} y = 0.2 \ &\rightarrow \widehat{\phi}_\gamma \simeq \pm 97.2^\circ\,, \ \ \widehat{\theta}_\gamma \simeq 20.6^\circ; \\ y = 0.4 \rightarrow \ &\widehat{\phi}_\gamma \simeq \pm 100.4^\circ\,, \widehat{\theta}_\gamma \simeq 24.9^\circ; \\ y = 0.6 \rightarrow \ &\widehat{\phi}_\gamma \simeq \pm 102.5^\circ,\ \widehat{\theta}_\gamma \simeq 25.2^\circ. \end{aligned} \tag{35}$$

It is straightforward to verify that the radiation dips, if projected onto the scattering plane, lie within the quadrants between the incoming (outgoing) e^+ and the outgoing (incoming) quark, the zone of destructive interference. As Fig. 3 shows, the radiation dips are clustered quite close to the (beam) direction of the incoming quark ($\theta_\gamma = 0^\circ$) which is particularly true for high–Q^2 events (back–scattered positron). As we have already pointed out, they are also within 10° (in θ_γ) of the final–state quark jet. However, they *are* well–separated from the outgoing particles when the ϕ_γ angle is taken into account. It will be very important to perform realistic simulations of these photon radiation events, including jet fragmentation and detector effects, to see whether the dips are indeed observable in practice.

Finally, in Fig. 9 we show the ϕ_γ dependence for slices through the $\widehat{\theta}_\gamma$ values of (35) which define the numerical location of the radiation dips of Fig. 3. We show the contributions of u quarks only, as well as the contributions from all light flavours (i.e. u, d and s quarks and antiquarks). At the critical values of $\widehat{\phi}_\gamma$ (again given in (35)) the obvious dips for pure u–quark scattering are somewhat filled in by the other 'background' (mainly d–quark) processes – the cross section at the bottom of the dip is increased by about two orders of magnitude – although they are still significant.

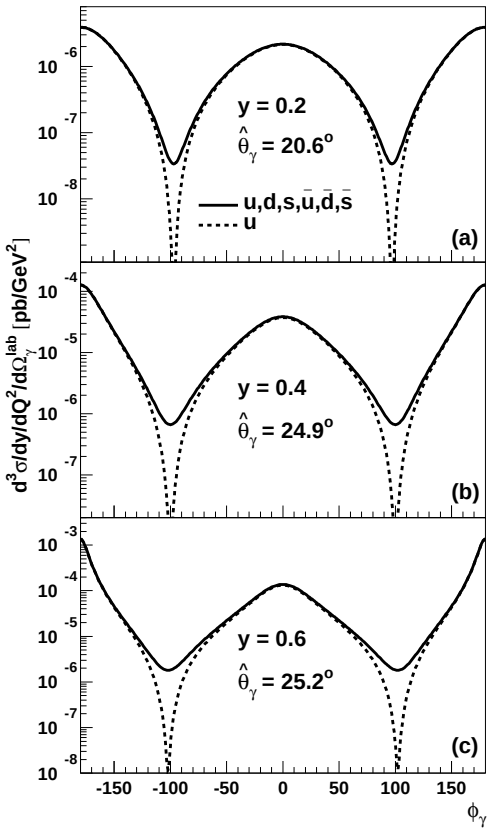

Fig. 9. The differential cross section of (31) for three different y values at the position of the radiation dips $\widehat{\theta}_\gamma$ shown in Fig. 3 as a function of the azimuthal angle ϕ_γ. We show the process $e^+u \to e^+u+\gamma$ (*dashed lines*) as well as the contribution (*solid lines*) of all light quark flavours (u, d, s quarks and antiquarks)

3.3 Radiation zeros and 'parton shower' models

To gauge the quantitative significance of the radiation zeros described in the previous sections, and in particular to factor out the effects of phase space constraints on the distributions, it is useful to make comparison with an approximate calculation in which radiation zeros are absent. Parton shower Monte Carlo programs, such as HERWIG [23] or PYTHIA [24], are based on the principle of the leading–pole (collinear) approximation. In particular they do not usually include the interference effects which are crucial for producing radiation zeros in the scattering amplitudes. We can easily emulate such models by removing the interference terms from the antenna pattern in (4) (i.e. the terms linear in e_q):

$$\frac{1}{2}\mathcal{F}_{\rm SM}^{\gamma\ \rm approx} = e_q^2[24] + [13], \tag{36}$$

The approximate matrix element thus obtained still contains the correct leading collinear singularities when the photon is emitted parallel to the incoming and outgoing quarks and leptons. In Fig. 10 we present the ratio

$$R_\gamma^u = \frac{d^3\sigma^{\rm approx}}{d^3\sigma}\left(e^+u \to e^+u+\gamma\right), \tag{37}$$

where $d^3\sigma^{\rm approx}/dydQ^2d\Omega_\gamma^{\rm lab}$ includes the antenna pattern without interference terms, as defined in (36). Again we slice through ϕ_γ at the values $\widehat{\theta}_\gamma$ of (35) where we numerically located the positions of the radiation dips for each y value. Note that away from the dips the ratio is $\mathcal{O}(1)$, as expected. However Fig. 10 also shows that close to the dips the approximate cross section is up to three orders of magnitude larger than the exact result, for all y values. In these particular regions of phase space, therefore, such 'parton–shower' models would dramatically overestimate the photon emission cross section.

4 Conclusions

The scattering amplitude for the process $eq \to qe+\gamma$ vanishes for certain configurations of the final–state momenta.

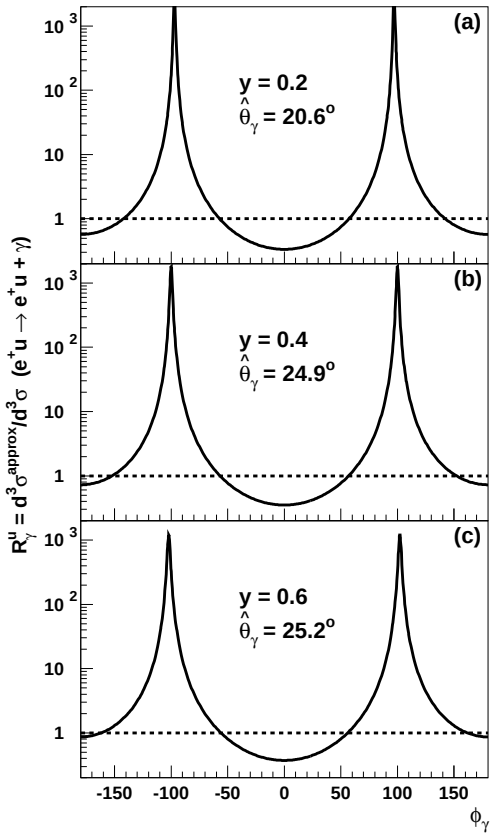

Fig. 10. Same as Fig. 9, but now for the process $e^+u \to e^+u+\gamma$ only. R^u_γ is the ratio of the differential cross sections of (31) without and with interference terms, see (37)

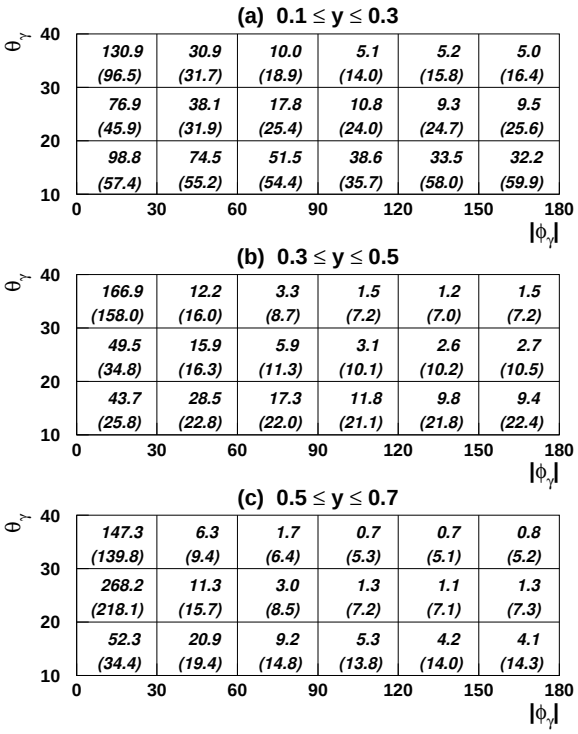

Fig. 11. The event rates $dN/d\Omega^{\rm lab}_\gamma$ for the production of e^+ + jet + γ mediated by the subprocess $e^+q \to e^+q+\gamma$ ($q = u(\bar{u}), d(\bar{d}), s(\bar{s})$) in three different y bins. We choose $x \in [0.1, 1]$ and this determines the range of Q^2 in a given y bin. We integrate the differential cross section of (31) over y, Q^2 and a given phase–space element $d\Omega^{\rm lab}_\gamma$ of the photon and assume an integrated luminosity $\int dt\mathcal{L} = 100$ pb^{-1}. The upper line in each bin shows the result of the exact calculation, and the lower line shows the results in the approximate calculation (employing the antenna pattern of (36) of Sect. 3.3). Note that we impose a 5° cut around the beam line and the outgoing positron and quark jet. The lower cut on the photon energy spectrum is again $\omega^{\rm cut}_\gamma = 5$ GeV

In this paper we have studied these radiation zeros and in particular their observability at HERA. In addition to the well-known class of (Type 1) same–charge zeros, which have been discussed in the pioneering work of [11-14], we have discovered a second class of (Type 2) zeros located in the eq scattering plane. We have so far been unable to find a theorem which leads to conditions for the existence of such zeros in more general scattering processes.

Experimentally, one might hope to be able to measure the four–momenta of the final–state lepton, quark (jet) and photon sufficiently accurately that the kinematic configurations which lead to zeros could be reconstructed. However a more realistic approach, which we have adopted here, is to study DIS + photon events for fixed lepton variables y and Q^2 and for a range of photon energies above a given threshold. This leads to sharp radiation dips instead of zeros. We performed such a study using the HERA lab frame. Although the radiation dips, i.e. the photon directions for which the cross section has a minimum, of both types are quite well separated from the beam direction and from the final–state jet, the e^+d scattering dips are completely swamped by the contributions from the other quark scattering processes. The e^+u (Type 1) dips offer a more promising hope of detection, since e^+u scattering is the dominant subprocess at high x.

Finally we address the question of whether the cross section dips can realistically be observed at HERA. For a given total luminosity, we can calculate the expected number of events with observable photons together with their distributions in solid angle, $dN/d\Omega^{\rm lab}_\gamma$. Fig. 11 shows the event numbers in bins of the photon angles θ_γ and $|\phi_\gamma|$ for the following cuts:

(a) $0.1 \le y \le 0.3$,
(b) $0.3 \le y \le 0.5$,
(c) $0.5 \le y \le 0.7$,

with $x \in [0.1, 1]$, a lower cut on the photon energy of $\omega^{\rm cut}_\gamma = 5$ GeV and an integrated luminosity $\int dt\mathcal{L} = 100$ pb^{-1}. Additionally we impose a 5° cut to separate the photon from the beam direction and the final–state positron and quark jet. For these cuts we find a total of (a) 2615.2, (b) 1723.2 and (c) 1237.4 $e^+ + {\rm jet} + \gamma$ events in

the three y bins respectively [4]. The two numbers in each bin in Fig. 11 correspond to the exact and approximate (as defined in Sect. 3.3, i.e. with *no* radiation zeros) matrix elements. Because of the y and x integrations and the finite bin size, the effect of the radiation zeros is smeared out. Nevertheless one can clearly see the expected suppression of the event rate in the exact case due to the presence of the Type 1 radiation zeros (in particular for $90^\circ < |\phi_\gamma| < 180^\circ$, as anticipated in Fig. 10). Furthermore the event rate (for this luminosity) does appear to be large enough for the effect to be observable.

We conclude, in agreement with [14], that the effect of radiation zeros should be visible at HERA.

Acknowledgements. We thank Bernd Löhr from the ZEUS Collaboration for fruitful discussions on various experimental aspects. We would also like to thank Stan Brodsky for drawing our attention to check the calculations for non–zero masses. MH gratefully acknowledges financial support in the form of a DAAD–Doktorandenstipendium (HSP III). WJS is grateful to the Fermilab Theory Group for hospitality during the completion of this work.

References

1. K.O. Mikaelian, D. Sahdev and M.A. Samuel, Phys. Rev. Lett. **43** (1979) 746
2. T.R. Grose and K.O. Mikaelian, Phys. Rev. **D23** (1981) 123
3. D. Benjamin for the CDF Collaboration, Proc. 10th Topical Workshop on Proton-Antiproton Collider Physics, Fermi National Accelerator Laboratory, Batavia, IL, May 9–13, 1995, preprint FERMILAB–CONF–95/241–E (1995)
4. U. Baur, T. Han, N. Kauer, R. Sobey and D. Zeppenfeld, Phys. Rev. **D56** (1997) 140
5. T. Abraha and M.A. Samuel, Oklahoma State U. preprint OSU–RN–326, hep-ph/9706336
6. J. Reid and M.A. Samuel, Prog. Theor. Phys. **76** (1986) 184
7. J. Reid and M.A. Samuel, Phys. Rev. **D39** (1989) 2046
8. K. Hagiwara, F. Halzen and F. Herzog, Phys. Lett. **B135** (1984) 324
9. R.W. Brown, talk presented at the International Symposium on Vector–Boson Self–Interactions, February 1995, Los Angeles (UCLA), hep-ph/9506018
10. S.J. Brodsky and R.W. Brown, Phys. Rev. Lett. **49** (1982) 966.
    S.J. Brodsky, R.W. Brown and K.L. Kowalski, Phys. Rev. **D28** (1983) 624.
    G. Passarino, Nucl. Phys. **B224** (1983) 265.
    M.L. Laursen, M.A. Samuel and A. Sen, Phys. Rev. **D28** (1983) 650.
    M.L. Laursen, M.A. Samuel, A. Sen and G.S. Sylvester, Phys. Rev. **D29** (1984) 994
    M.L. Laursen, M.A. Samuel, A. Sen and G.S. Sylvester, Phys. Rev. **D31** (1985) 1657
11. C.L. Bilchak, J. Phys. **G11** (1985) 1117
12. G. Couture, Phys. Rev. **D39** (1989) 2527
13. G. Li, J. Reid and M.A. Samuel, Phys. Rev. **D41** (1990) 1675
14. M.A. Doncheski and F. Halzen, Z. Phys. **C52** (1991) 673
15. M. Heyssler and W.J. Stirling, Phys. Lett. **B407** (1997) 259
16. H1 Collaboration: C. Adloff et al., Z. Phys. **C74** (1997) 191
17. ZEUS Collaboration: J. Breitweg et al., Z. Phys. **C74** (1997) 207
18. F.A. Berends, R. Kleiss, P. De Causmaecker, R. Gastmans and T.T. Wu, Phys. Lett. **B103** (1981) 124
19. M. Heyssler and W.J. Stirling, Durham preprint DTP/97/102, hep-ph/9712314
20. ZEUS Collaboration: M. Derrick et al., Z. Phys. **C65** (1995) 379
21. H1 Collaboration: T. Ahmed et al., Nucl. Phys. **B439** (1995) 471
22. A.D. Martin, R.G. Roberts and W.J. Stirling, Phys. Lett. **B354** (1995) 155
23. G. Marchesini, B.R. Webber, G. Abbiendi, I.G. Knowles, M.H. Seymour and L. Stanco, Comp. Phys. Comm. **67** (1992) 465
24. T. Sjöstrand, Comp. Phys. Comm. **82** (1994) 74

[4] Note that the *total* $e^+ +$ jet rate for these bins is approximately two orders of magnitude larger